DOI: 10.13009/EUCASS2017-215

Micro-Aerothermodynamics Analysis of the SpaceLiner Cabin Escape System along Atmospheric Re-entry

E.Laroche, Y.Prévereaud*, J.-L.Vérant*, M.Sippel**, D.Bonetti****
**ONERA – The French Aerospace Laboratory*
2 avenue Edouard Belin – 31055 Toulouse – France
***DLR – SART*
Robert-Hooke-Straße 7 – 28359 Bremen – Germany
****DEIMOS elecnor group*
Ronda de Poniente 19, Edificación Fiteni VI – 28760 Tres Cantos (Madrid) – Spain

Abstract

This paper focuses on the analysis of the aerothermodynamic phenomena encountered by the escape cabin of the SpaceLiner vehicle [6] along its re-entry trajectory. Two flight configuration issues have been yet considered. Firstly, the deployment of the inflatable system is investigated using a transient simulation based on a mesh deformation methodology for a Mach 20 in-flight condition. Secondly, micro-aerothermodynamic simulations of a realistic vehicle including technological elements like gaps, folding cavities for rudders, stiffeners for flaps, jettisoning thrusters were performed, exhibiting major influences compared to a pre-flight "smooth" configuration.

1. Introduction

Passenger safety is one of the key issues for the development of future trans-atmospheric hypersonic transportation systems such as the SpaceLiner concept (Figure 1), which has been investigated by the DLR since 2005 [1]. The SpaceLiner is a rocket-propelled suborbital craft based on two stage reusable launch vehicles (RLV) allowing to transport up to 100 passengers [2] from Australia to Europe within 90 minutes. The last version of the SpaceLiner (version 7-3) is presented in Figure 1[3], [6]. The reusable booster and the passenger stage are attached thanks to a classical tripod. The reusable booster is 82.3 m in length, 36 m in span, 8.7 m in height with a diameter of 8.6 m. The passenger stage is 65.6 m in length, 33 m in span, 12.1m in height with a diameter of 6.4 m [3]. In case of catastrophic event, passengers must be moved to safety as easily and quickly as possible. So, the passenger cabin serves as pressurized travel compartment and reliable rescue system in case of flight abort. It is 15.6 m in length and 5.6 m in height. However, the implementation of a cabin escape system for a hypersonic aircraft is challenged by the investigation within a larger structure, the load factors for the passengers, the ejection propulsion concept, the capability to withstand the extreme aerothermodynamics environment, the adaptability to a wide range of abort scenario conditions and the capacity to fly autonomously back to Earth's surface.

A cabin escape system able to change its shape and automatically reconfigure during an abort event after ejection could be a good compromise between the constraints for the integration within the mother-spacecraft, the adaptability to the unpredicted environment in case of abort and the required flight performance to ensure safe landing. The objective of the EU funded HYPMOCES program (HYPersonic MOrphing for a Cabin Escape System) was to address key technological areas to enable the use of morphing in hypersonic escape systems, such as control and reconfiguration during morphing, structures, materials, actuators and mechanism of the deployed elements, compliance with system integration with the escape system and the mother aircraft, and aerothermodynamics (ATD) issues of the changing external shape. Inside this framework, ONERA is specifically responsible for the delivery of the detailed AeroThermodynamics Data Base (AETDB) used to define a satisfactory design. Indeed, two key issues are the trajectory and the stability of the escape vehicle and its ability to withstand the critical levels of heat fluxes encountered during the Earth atmospheric re-entry. Guidance, Navigation and Control (GNC) engineers and structural design team are end-users of this database. A preliminary database, which had conducted to the definition of the final design, was presented in [4]. In the second part of the HYPMOCES project, two flight configuration issues have been considered for the critical flight point from an aerothermodynamics point of view. First, the deployment of the inflatable system is analysed using a transient simulation approach based on a mesh deformation

DOI: 10.13009/EUCASS2017-215

methodology (section 3). Secondly, micro-aerothermodynamic simulations of a realistic flight vehicle including technological elements like gaps, folding cavities for rudders, stiffeners for flaps, jettisoning thrusters were performed (section 4). For the cases presented in this paper, computations are performed at Mach 20 ($V = 6314$ m/s), at an altitude of 57.8 km ($T_\infty = 253.07$ K and $P_\infty = 29.5$ Pa). This flight point corresponds to the point where the heat flux received by the wall is maximum. The vehicle is assumed to have a flaps deflection of +15°, with an angle of attack of 10° and no side slip angle.

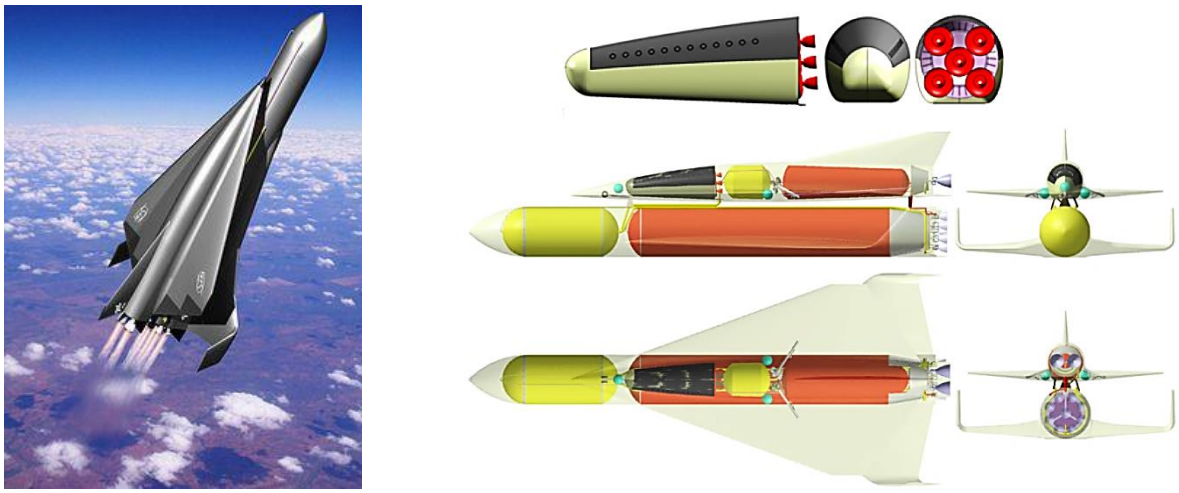

Figure 1. Views of the SpaceLiner laucher system with booster stage and the passenger/rescue cabin as designed by DLR [3]

3. Influence of the vehicle local shape modification: transient analysis

One of the main questions arising during the deployment of the inflatable system is that of the time evolution of heating. As a matter of fact, the potential existence of a transient overshoot phenomena would make the use of the fully-deployed configuration inappropriate or irrelevant for sizing considerations.

3.1 Morphing process

The morphing process under consideration corresponds to the deployment of inflated wings and was designed by AVIOSPACE partner. The deployment process will be described numerically through a mesh deformation approach. This technique allows to update at each iteration the information related to the mesh, taking into account the boundary nodes displacements. The algorithm used will be developed in next paragraph 3.2. Figure 2 illustrates the changes in geometry induced by the inflating process. The wing deployment from *Undeployed* to *Deployed* configuration takes place during 2 seconds. The changes can be considered as significant regarding the characteristic lengths of the vehicle, but are still moderate with respect to the volume mesh around the vehicle. In particular one can think that the update of the volume mesh propagating the boundary nodes displacements will be feasible. Taking into account the intensive CPU requirements of the simulation, only 0.4 s were simulated, which correspond to 20% of the inflated wings displacement. However, this shorter duration than given requirement allows characterizing the expected potential overshoots and, therefore addresses one the major objectives of this simulation.

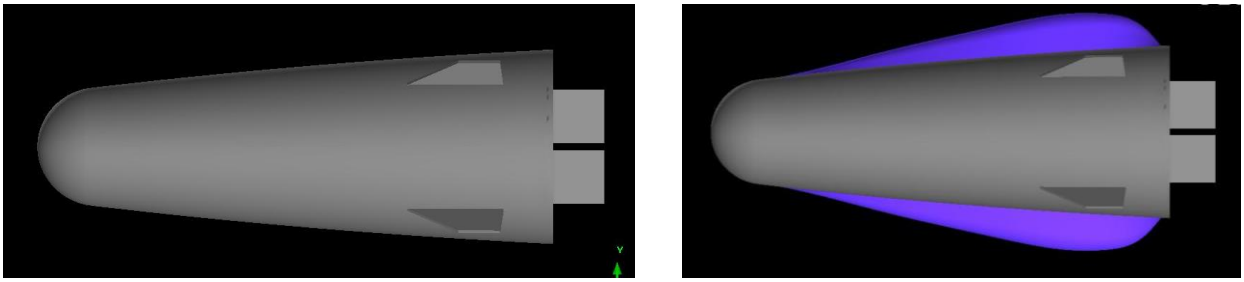

a) *Undeployed* b) *Deployed*

Figure 2. Initial and final geometries considered

DOI: 10.13009/EUCASS2017-215

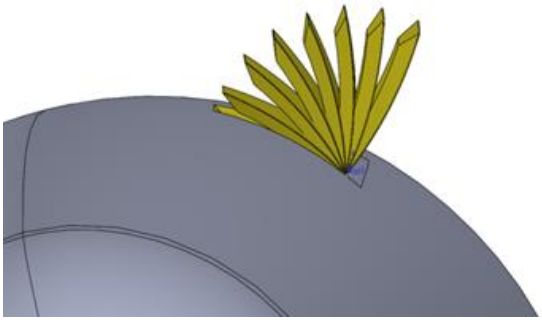

Figure 3. Rudder deployment sequence

Here, the rudder dynamic deployment will not be considered. As a matter of fact, this would require to start the calculation from an initially small gap between the rudder and the vehicle (folded conf.), inducing strongly 'drag' on the mesh (within a very small volume) to take the deployment process into account (Figure 3). The rudders were then assumed as fully deployed during the inflated wing deployment process.

3.2 Algorithm used

A discretization of the surface is defined at the initial reference time (start point). The same discretization connectivity is used to discretize the surface at the final time of the deployment. The connectivity is assumed to be the same through the deployment process, and the geometric transformation is assumed to be linear in time between two coupling processes. These coupling times are 0 and 2 seconds. The simulation is performed using an external coupling between ONERA CFD code CEDRE and a mechanical emulator called CATALPA. During the process, CATALPA prescribes the node displacements to CEDRE and CEDRE potentially sends the pressure information to CATALPA. This pressure information is not used here. The node updates are calculated at prescribed coupling times. Then a linear interpolation of displacements is assumed between 2 couplings. The CPU penalty due to mesh updates quantities is 0.25 time the reference iteration time. This penalty corresponds to the update of all mesh information taking into account the estimate of the distance to the wall.

During computations, CEDRE evaluates at each time a new surface mesh motion interpolated on the basis of the discretized surface. This mesh is used by the mechanical emulator CATALPA. Then each CEDRE surface node motion is interpolated onto this mesh to determine the node displacement. The inner nodes are then moved based on a predefined law, and an updated solution is computed. Then, the calculation is continued or ended according to schematic (Figure 4).

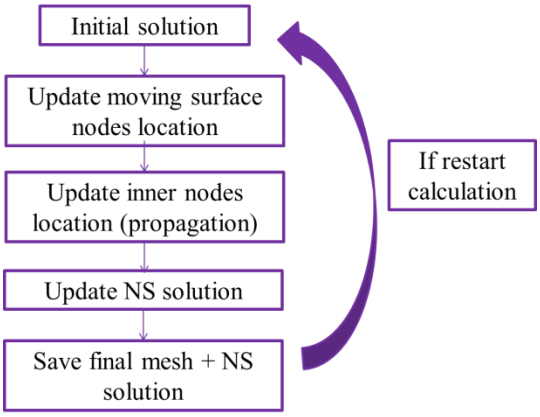

Figure 4. Transient algorithm

3.3 Definition of the initial solution

The calculation starts from the *Undeployed* configuration whose CAD was provided by DLR. A Navier-Stokes steady-state solution of this configuration is the starting point of the transient simulation. The main elements regarding mesh generation and characteristics of such stationary solution are described below.

DOI: 10.13009/EUCASS2017-215

3.3.1 Mesh generation

A mesh cut can be visualized in Figure 5. The generated mesh is made of tetrahedra, prisms (wall and shock regions) and pyramids (interface between tetrahedral and prisms). The prisms in the wall region are dedicated to a correct description of the boundary layer. The prisms in the bow shock region allow a better capture of the strong shock. As a matter of fact, the capture of bow shocks with tetrahedral elements can lead to numerical stiffness that can be alleviated with the use of prisms. The final mesh is made of 8.8 million elements. The inlet surface comes from a first calculation on a coarse mesh. The bow shock location is then estimated and this surface is shifted to be able to grow at least to 4 prisms layers.

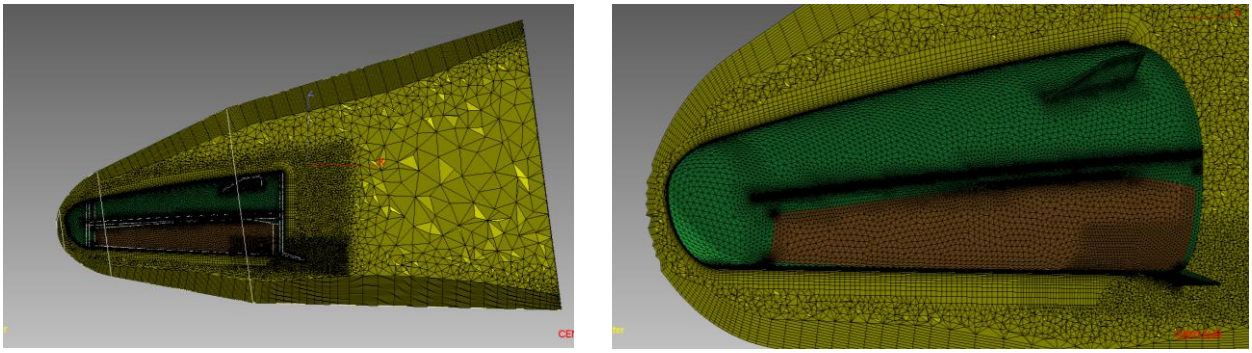

a) b)

Figure 5. *Undeployed* mesh [(a) overview, (b) zoom]

3.3.2 Steady-state solution

The steady-state solution is displayed on Figure 6. The level of convergence has to be high in the sense that the modifications carried out by the moving surface displacement will be small compared to the gradients present in the Navier-Stokes steady-state solution. Any convergence error could be wrongly attributed to the membrane displacement. This convergence required 22000 iterations, with 12000 iterations at CFL = 1.

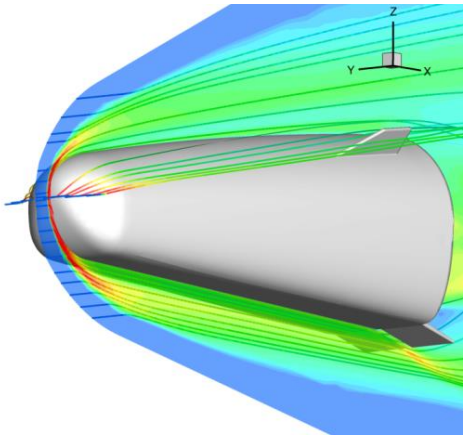

Figure 6. *Undeployed* configuration with Navier-Stokes steady-state solution (Temperature field, streamlines coloured by temperature)

3.4 Result analysis

The inflating process simulation is carried out during $400\,ms$ due to intensive CPU requirements. The inflating geometry can be visualized on Figure 7. The simulation is time-resolved, with a time step used of 5 µs ($0-200\,ms$) and 10 µs ($200-400\,ms$). The CPU return time is about 15 h for $100\,ms$ on a 420 cores cluster (equivalent to 6300 CPU hours on one processor). Regarding the time step retained, it corresponds to a maximum displacement during the time step of around 10 µm, which one order higher than the wall cell size (1 µm) but very small compared to the characteristic sizes of the whole vehicle (15m).
The evolution of the transient heat flux, calculated at radiative equilibrium wall condition, assuming a fully catalytic wall, can be exhibited in Figure 8 and Figure 9. Far from the moving surface, no major evolution can be observed in

DOI: 10.13009/EUCASS2017-215

the leeward region. In the windward region, the heat flux level is gradually decreasing in regions where the curvature radius increases, whereas it increases in regions where the curvature radius decreases. This observation is consistent with what it is expected. In particular, in the aft region of the membrane which is more deformed than the front, the blue region indicates a reduced level of heat flux.

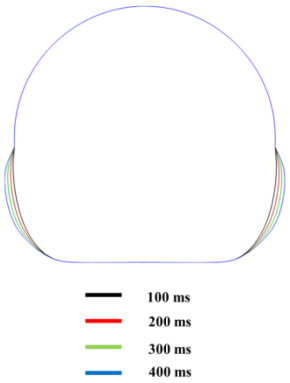

Figure 7. Inflating geometry evolution

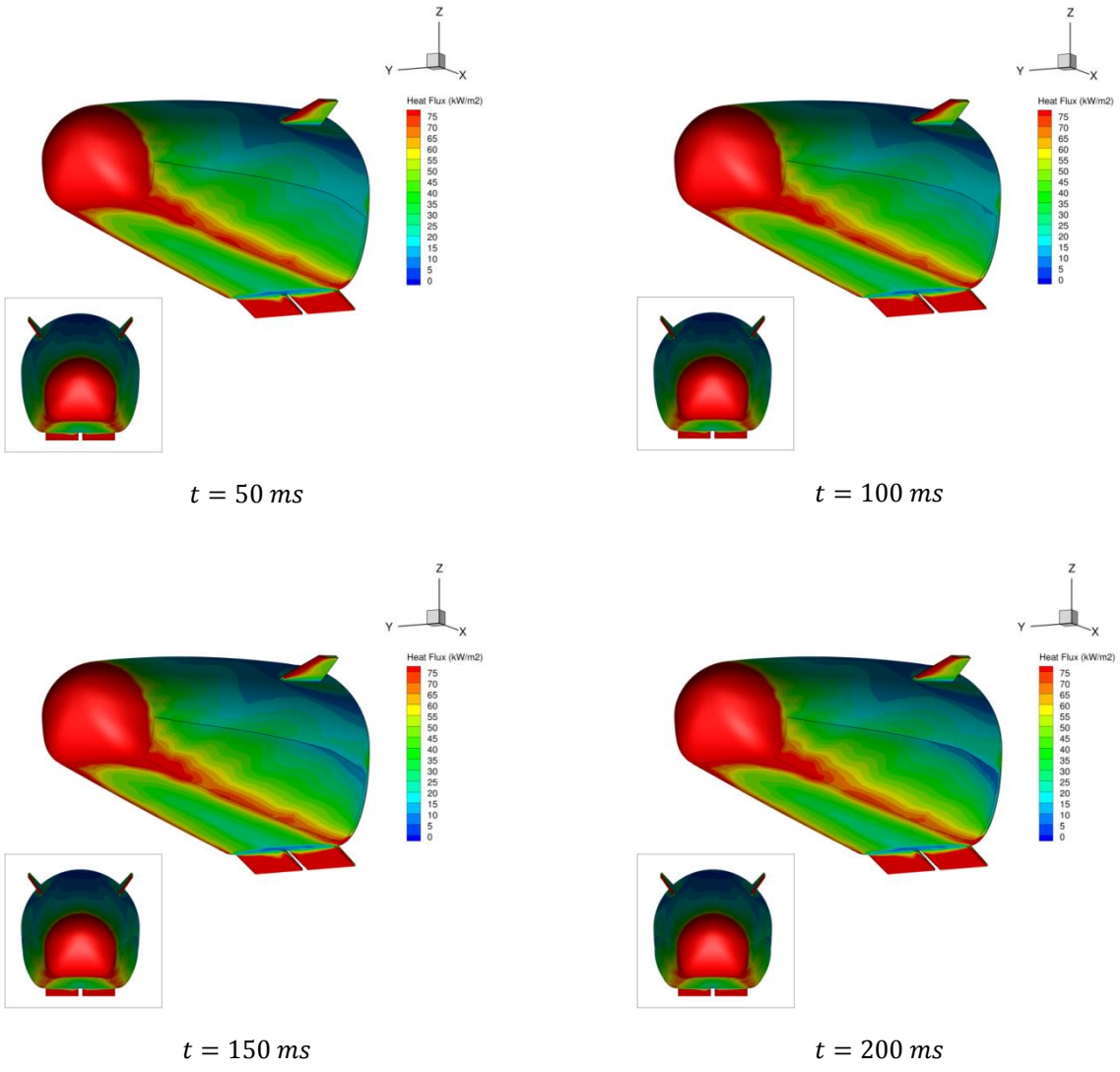

$t = 50\ ms$ $t = 100\ ms$

$t = 150\ ms$ $t = 200\ ms$

Figure 8. Heat Flux time evolution ($0 - 200\ ms$)

DOI: 10.13009/EUCASS2017-215

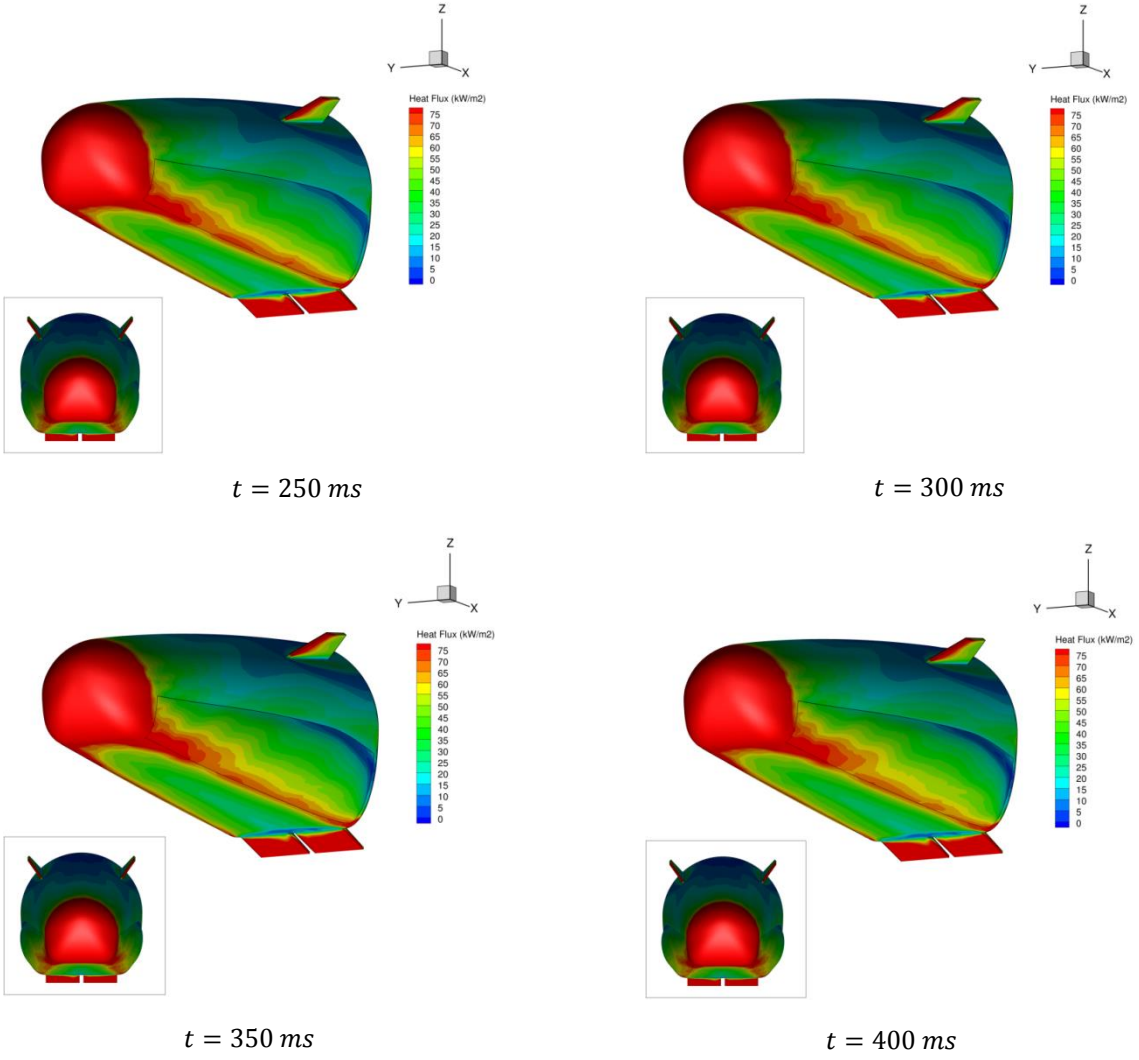

Figure 9. Heat Flux time evolution ($200 - 400\ ms$)

Another noticeable observation is the absence of overshoot of heat flux level along the morphing process. The time evolution of heat flux is smooth, which was estimated highly probable accounting for the time scale of the morphing (2s) and compared to the flow time characteristics (order of magnitude below). One can also observe slight variations of the heat flux level in the flap vicinity. This seems to be an indirect effect of the morphing process.

Coming to sizing issues, the calculation confirms that the *Undeployed* and fully *Deployed* geometry provide two points that can be considered as sizing in terms of heating levels. For any point, a linear evolution of the heat flux between those two points seems to provide a reasonable estimate of the expected value.

4. Aerothermodynamic analysis of the flight vehicle

The objective is to assess the influence of the flight geometry including thrusters, wings and flaps hinges on the flow topology and thus on the pressure, aerodynamic coefficients and heat flux distribution. Moreover, two kinds of rudders cavities have been investigated (Figure 14 and Figure 15). The present configuration is *deployed* regarding inflatable elements.

4.1 Mesh strategy

The mesh of the complete geometry, generated with the CENTAUR software, is an hybrid 3D mesh (tetrahedral and prisms) made of 32 million nodes and 90 million elements. Several layers of prismatic cells have been built at the wall to properly capture gradients (Figure 10). The first layer consists of 1 µm elements, the others increasing by a

DOI: 10.13009/EUCASS2017-215

ratio of 1.25. The mesh has been designed and refined to include the bow shock into prisms zone, as well as the afterbody recirculation zone and detachment/reattachment phenomena occurring in the flap region (Figure 10 and Figure 11). Surface mesh presents several refinement zones (Figure 12) to correctly describe the wall curvature and small surfaces such as around the gaps and the leading edges of the rudders (Figure 14 and Figure 15), the thrusters (Figure 16), the detailed backward design of the flaps (Figure 17) and the gaps themselves allowing the deployment of the inflatable system (Figure 13).

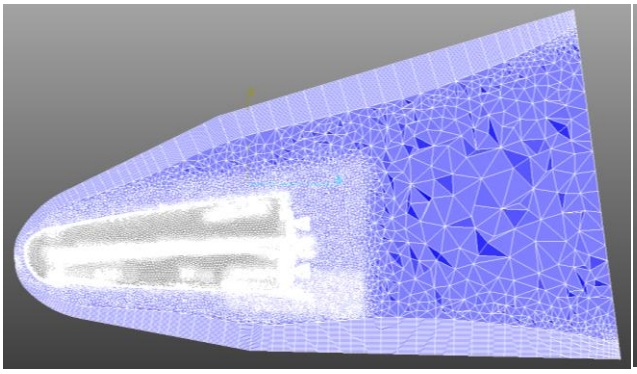

Figure 10. view of the 3D mesh realised around the complete geometry with δ = 15°

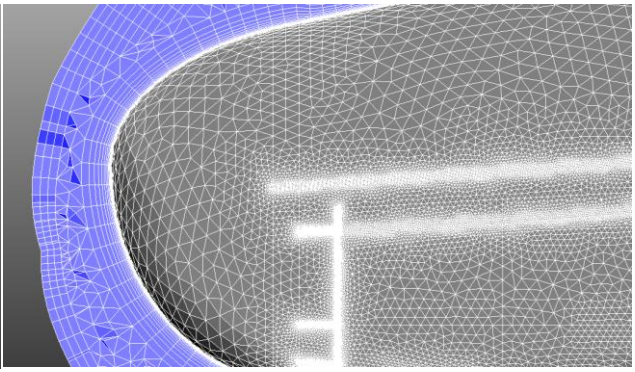

Figure 11. view of the 3D mesh nearby the nose of the complete geometry

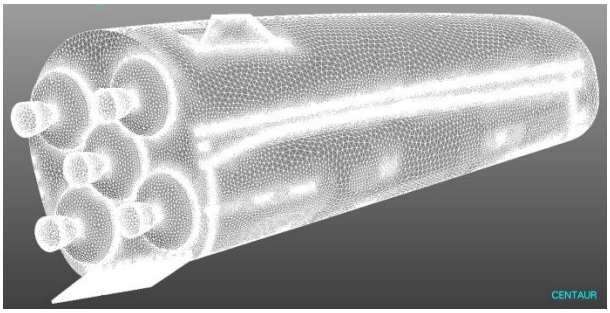

Figure 12. View of the surface mesh obtained around the complete geometry with δ = 15°

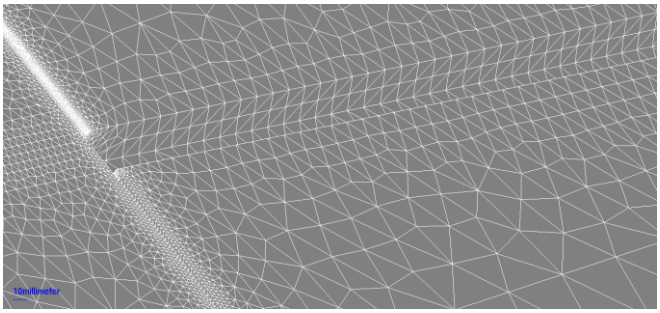

Figure 13. Mesh of the gaps surrounding inflatable elements

4.2. Computation setup

CFD computations of the complete geometry have been conducted with the ONERA unstructured Navier-Stokes solver CHARME as previously described and using a chemical non-equilibrium model based on Park's kinetics to assume real gas effect occurring at Mach 20. The Navier-Stokes equations have been resolved with a second-order finite-volume discretization in space, with the flux vector splitting AUSM+ scheme associated to a MinMod limiter. The time integration has been set to a one-step fully implicit approach. No turbulence model has been employed since laminar status of the flow is expected at Mach 20 and at such high altitude. The walls of the complete geometry are considered firstly as fully catalytic with an emissivity of 0.8 and partly non-catalytic for the nose and inflated elements in a second computation (presented in paragraph 4.5). The wall heat flux is calculated assuming radiative equilibrium.

Fully catalytic computation has been running on 480 processors during ~200 hours, corresponding to around 94 000 CPU hours on one processor. With a time step of 10 µs, it corresponds to 40 500 iterations on 480 processors.

4.3 Analysis of the flow topology

Figure 18 presents a general overview of the flow topology around the detailed vehicle configuration. The friction lines from the leeward and the flanks of the vehicle gather and form an important recirculation zone in the vehicle wakeflow (Figure 19). The flow temperature of the recirculation zone can reach almost 5000 K at specific location (where the shear layers gather and wake shock begins). The vehicle base surface should increase its total heating by the Radiative Heat Transfer (RHT) contribution due to the high temperature wake flow node. However, RHT is not considered in the present computations conducted and its effect of sizing or not for the base protection material should be investigated in further investigations. The flow topology around the inflatable systems does not show any

DOI: 10.13009/EUCASS2017-215

recirculation zone, especially ahead of the end of the vehicle (Figure 20). The size of the gap has a limited influence on the flow topology around the rudders (Figure 21 and Figure 22).

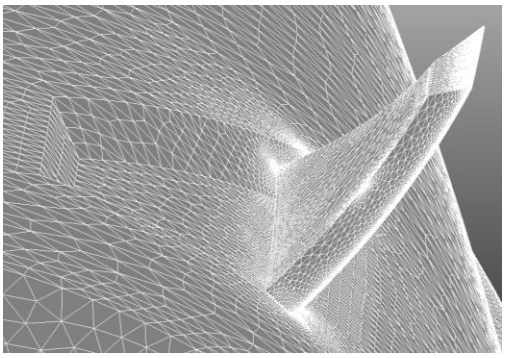

Figure 14. Mesh of the rudders and the folding cavity (design 1) after deployment

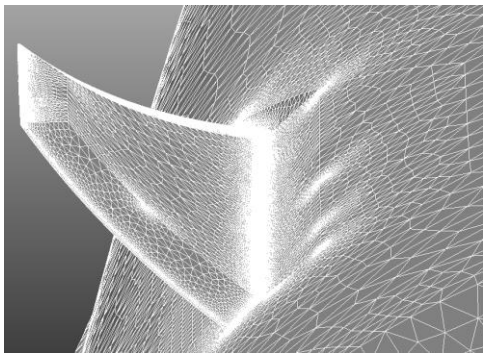

Figure 15. Mesh of the rudders and the folding cavity (design 2) after deployment

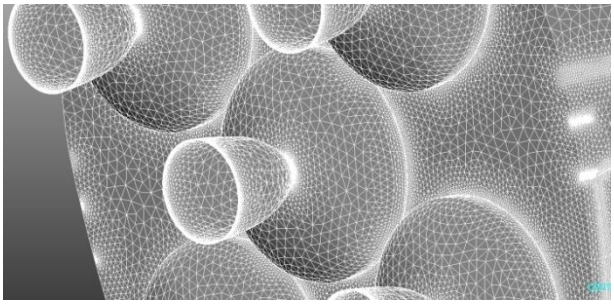

Figure 16. Mesh of the thrusters

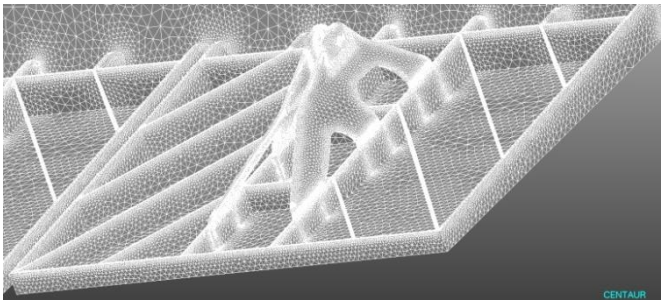

Figure 17. Detailed mesh of the backward flaps surface (leeward view)

Windward gaps, inserted into the Thermal Protection System material and allowing the deployment of the inflatable system, have a significant influence on the flow topology on the flaps. The gaps begin nearby the nose and drive the streamlines until the flaps where they induce an important heterogeneous flow detachment (Figure 23). The temperature of separation and re-attachment flow can reach almost 5000K as a stagnation zone (Figure 24). However, at the wall the temperature will be cooler even though re-attachment always induces high heating conditions. Finally, small and heterogeneous recirculation zones develop between the flaps hinges except in the vicinity of the centre of the vehicle (Figure 25).

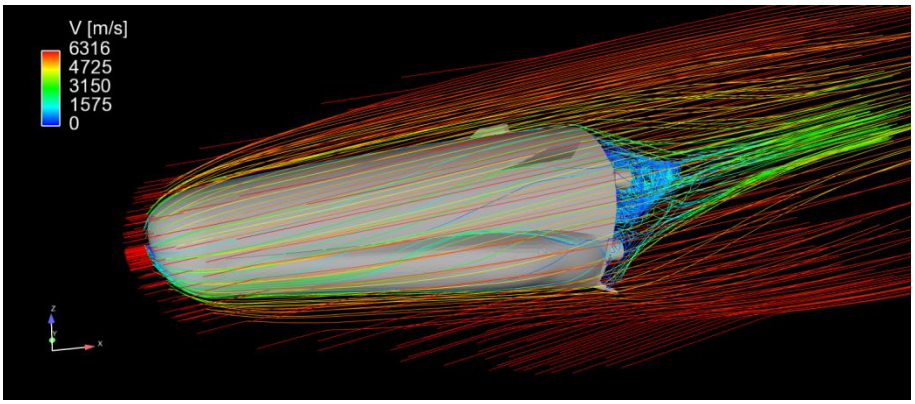

Figure 18. Flow topology around the detailed vehicle geometry

DOI: 10.13009/EUCASS2017-215

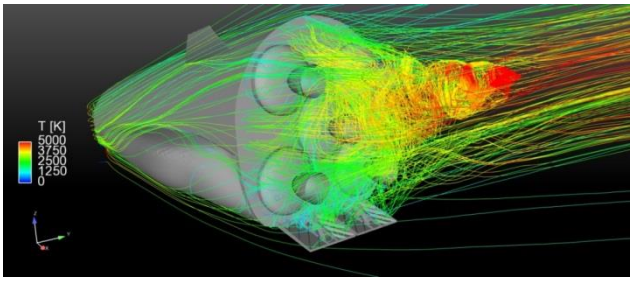

Figure 19. Temperature in the wake flow

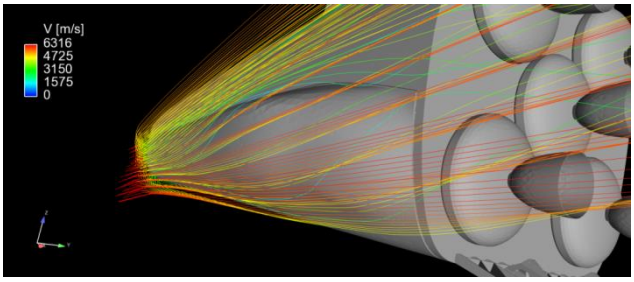

Figure 20. Flow topology around the inflatable system of the detailed vehicle geometry

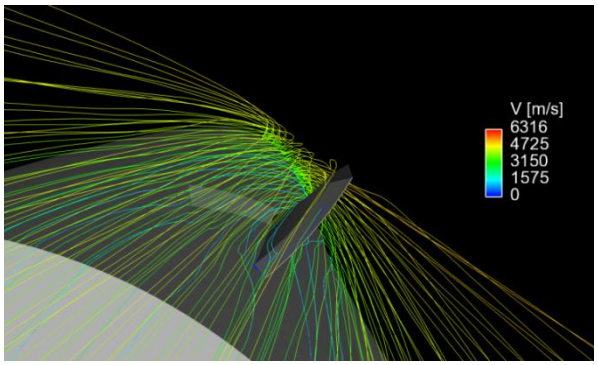

Figure 21. Flow topology around the rudders (with large cavity) on the leeside of the detailed vehicle geometry

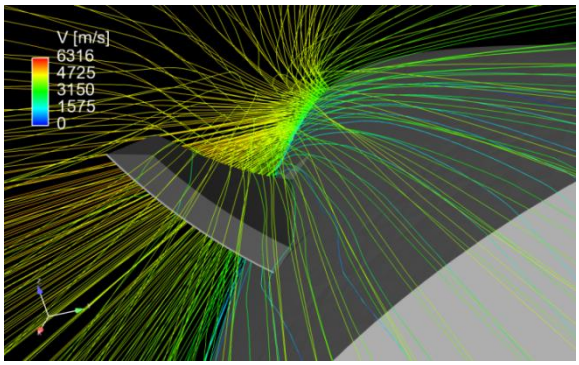

Figure 22. Flow topology around the rudders (with reduced cavity) of the detailed vehicle geometry

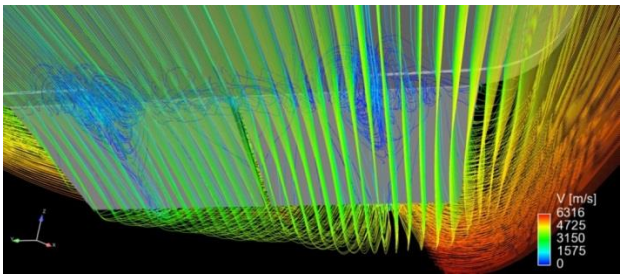

Figure 23. Flow topology (streamlines) in the flaps area of the detailed vehicle geometry

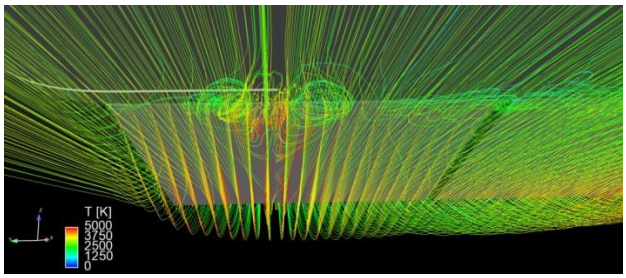

Figure 24. Temperature of the flow (colorized streamlines) in the flaps area of the detailed vehicle geometry

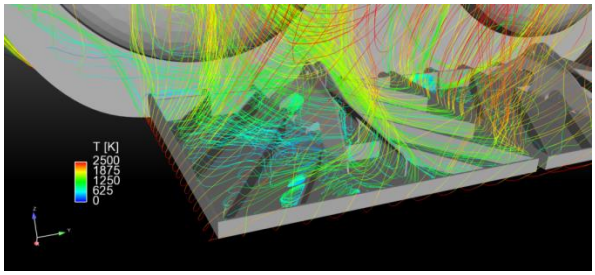

Figure 25. Temperature of the flow (colorized streamlines) at the back of flaps of the detailed vehicle geometry

DOI: 10.13009/EUCASS2017-215

4.4 Analysis of the wall heat flux distribution and wall temperature

Figure 26 shows the total heat flux distribution on the vehicle surface. The maximum stagnation point heat flux is around 808 kW/m². The average heat load on the entire inflatable system achieves a maximum value of 52 kW/m², except in the vicinity of the nose, where it reaches 181 kW/m² (Figure 27). The mean temperature on the wall of the inflatable system is around 1000 K and a peak of temperature is noticed nearby the nose (1422 K), as plotted on Figure 28.

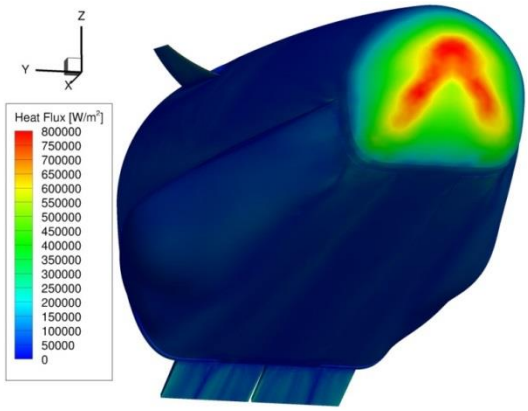

Figure 26. Heat flux around the nose of the detailed geometry

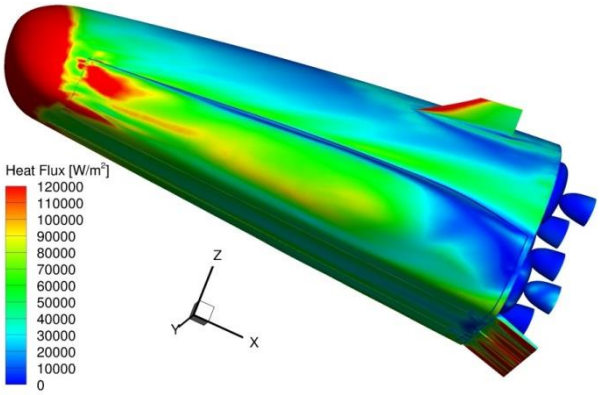

Figure 27. Heat flux on the left side (pilot view) of the detailed geometry

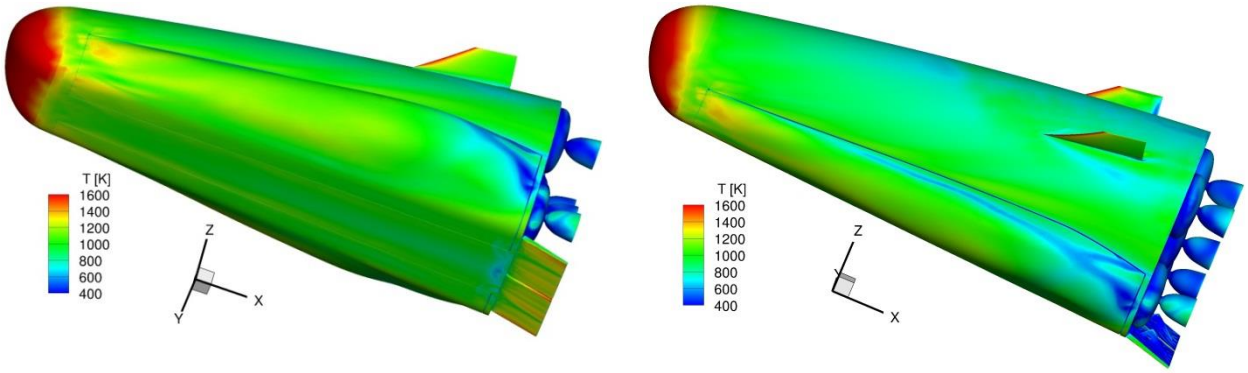

Figure 28. Wall temperature around the inflatable system on the left side (pilot view) of the detailed geometry

The heat flux on the rudders leading edge remains between 1500 and 2000 kW/m² (Figure 29). These values appear to be excessive and unrealistic. It is mainly due to the difficulties to characterize accurately the heating of a very small curvature radius of a very thin leading edge ($r = 5\ mm$). Therefore, gradients are incorrectly captured leading to excessive computed values. Increasing the number of cells in this specific region would involve a dramatic increase of cells by cascade effect and final mesh would be far beyond present 90 million cells, already a unique challenge for hypersonic and high temperature simulation.
The size of the rudders cavities modifies the wall heat flux distribution in their neighbourhood (Figure 29). However, one must remind that the heat flux in the rudders cavity achieves only 93 kW/m², which is quite low compared to the stagnation point heat flux.

DOI: 10.13009/EUCASS2017-215

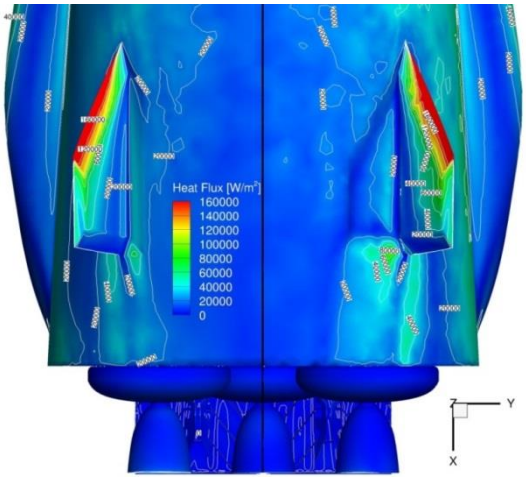

Figure 29. Heat flux distribution around the rudders for the two kinds of cavities studied

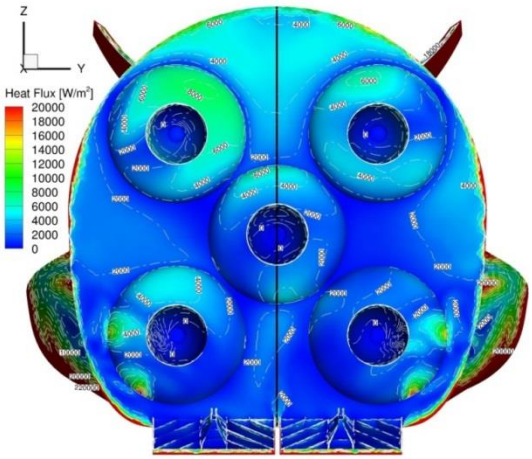

Figure 30. Heat flux distribution around the thrusters on the base of the detailed vehicle (asymmetrical flow patterns due to different rudders cavities)

The rudders cavities have also an influence on the recirculation zone topology, since the heat flux distribution on the thrusters located on the top of the vehicle is impacted (Figure 30). A smaller rudder cavity induces a slightly higher heat flux, since the computed flux is around 8 kW/m² on the left side thrusters of the vehicle whereas a value of 6 kW/m² is obtained on the right side (Figure 30). Moreover, the flow skirting the inflatable systems impacts the lower thrusters inducing an observable peak of heat flux, that reaches 20 kW/m².

The wall heat flux and temperature on the flaps are depicted in Figure 31 and Figure 32 respectively. The specific flow topology induced by the longitudinal gaps of the inflatable system has a significant impact on the characteristics of the heat flux distribution on the flaps as previously mentioned. The recirculation zone without homogeneous re-attachment zone leads to the presence of longitudinal cooled zones on the flaps. The wall temperature is then between 850 and 1570 K. The slight flow asymmetry observed on the flaps (Figure 31) is due to the asymmetry of the unstructured mesh.
Inside the flaps hinges, a cooling process is active where recirculation zones are developed. However, the heat flux remains lower to 2 kW/m² (Figure 33). The proportion of radiative heat flux from a wall to another is not taken into account but will increase the evaluated heat flux levels. Between the two flaps, the thermo-mechanical constraints can be significant. The temperature on the side of the flap can reach 1510 K (Figure 34).

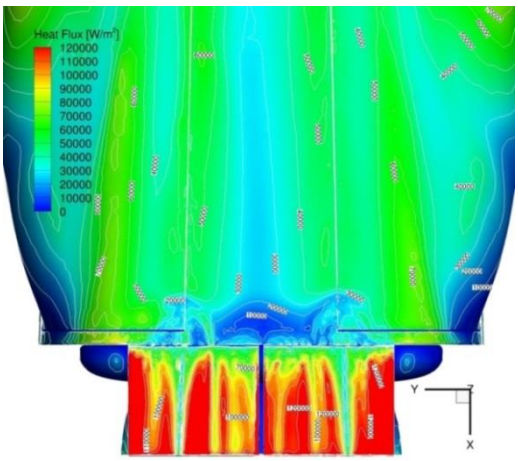

Figure 31: Heat flux distribution in the neighbourhood of the flaps of the detailed geometry.

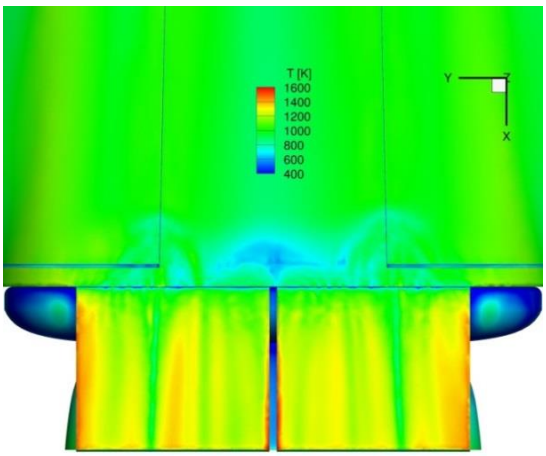

Figure 32: Wall temperature in the neighbourhood of the flaps of the detailed geometry.

DOI: 10.13009/EUCASS2017-215

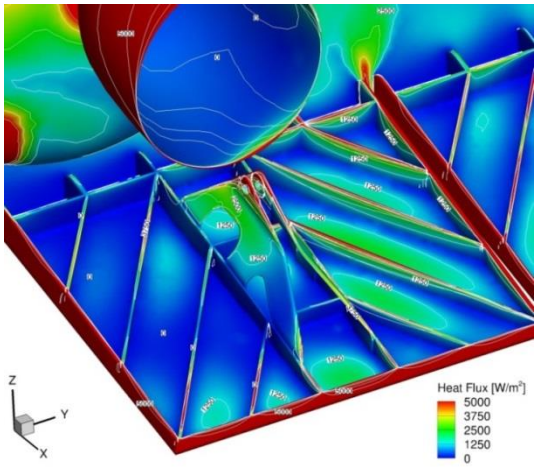

Figure 33: Heat flux distribution inside the backside of the flaps of the detailed geometry (stiffeners).

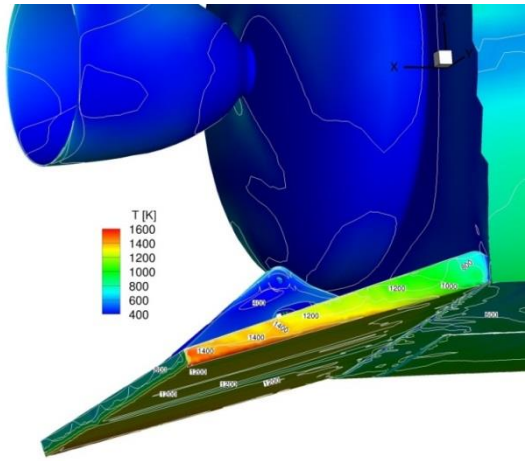

Figure 34: Wall temperature on the thickness of flaps of the detailed geometry.

4.5 Analysis of the influence of the catalycity for inflatable elements heating

4.5.1 Computational setup

Computational parameters and mesh are strictly identical to the ones used for the calculation around the detailed geometry as displayed above. Only the wall catalycity condition is modified. Since materials used for the different parts of the vehicle have different catalytic properties, it appears interesting to simulate a configuration where the nose and the inflatable system are considered as non-catalytic. Other surfaces of the vehicle are then considered as fully catalytic (Figure 35). ATDB is usually developed assuming a fully catalytic surface for the whole vehicle to size properly heating loads whatever chosen TPS, often close-to-non catalytic material.

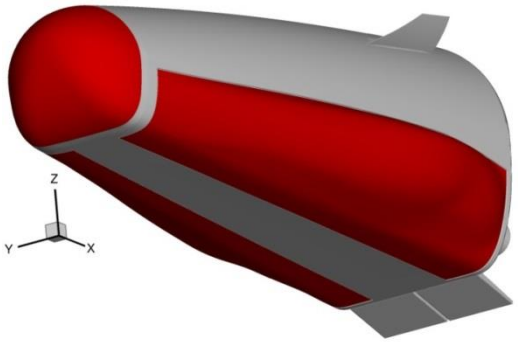

Figure 35: Highlight of full catalytic (in grey) and non-catalytic walls (in red).

4.5.2 Analysis of the influence of the wall catalycity on the wall heat flux

The wall catalycity property has a strong but expected influence on the heat flux distribution (Figure 36, Figure 37 and Figure 38). Indeed, the maximum heat flux at stagnation point is lower by 46% in the case of a non-catalytic wall than in the case of a full catalytic wall. The stagnation point radiative equilibrium temperature is around 2080 K for a catalytic wall against 1762 K for a non catalytic wall, corresponding to a difference of more than 15% (Table 1). On the inflatable system (Figure 37), the mean heat flux is around 52 kW/m² with a catalytic wall vs. 22 kW/m² with a non-catalytic wall.
Finally, as can be observed on Figure 38, a local peak heat flux appears between the nose and the inflatable system assuming a non-catalytic wall. The different properties interfaces between catalytic and non-catalytic surfaces (between nose and the rest of the vehicle or between the inflatable system and the rest of the vehicle) induce a modification of the boundary layer and thus a local increase of the heat flux that was noticed in the past concerning catalycity change on RLV (Reusable Launch Vehicle) thermal protection systems [5].

DOI: 10.13009/EUCASS2017-215

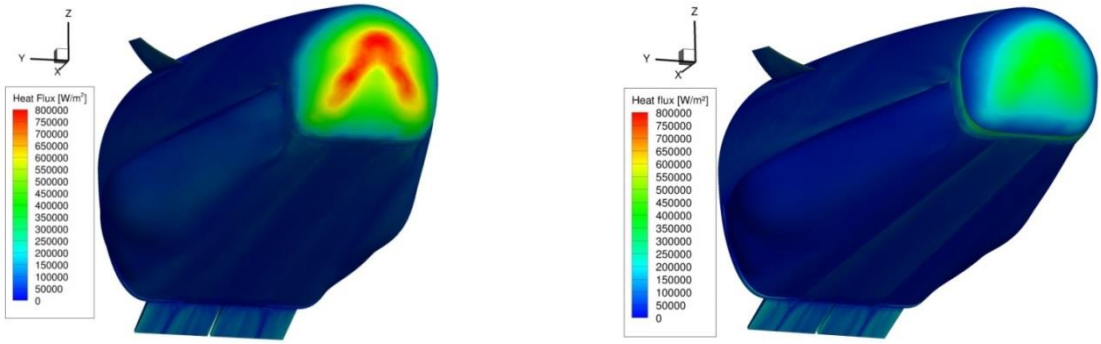

Catalytic wall Non-catalytic wall

Figure 36: Influence of the wall catalycity on the heat flux distribution in the neighbourhood of the nose of the detailed geometry.

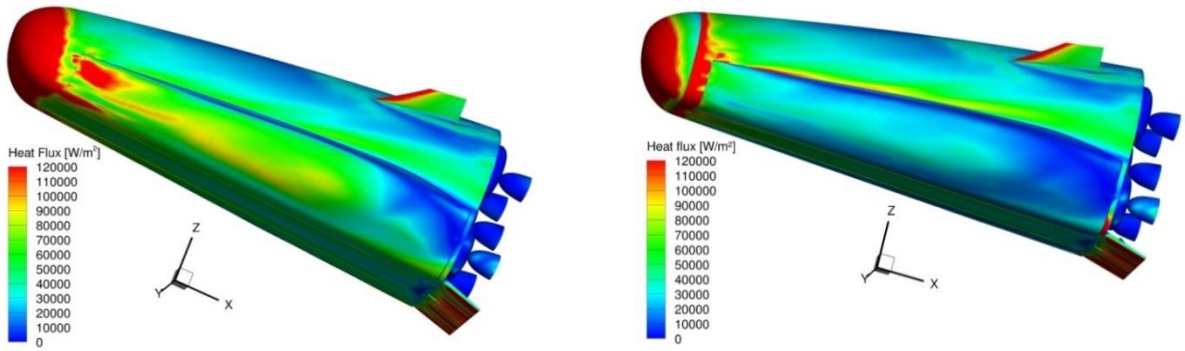

Catalytic wall Non-catalytic wall

Figure 37: Influence of the wall catalycity on the heat flux distribution on the inflatable system of the detailed geometry.

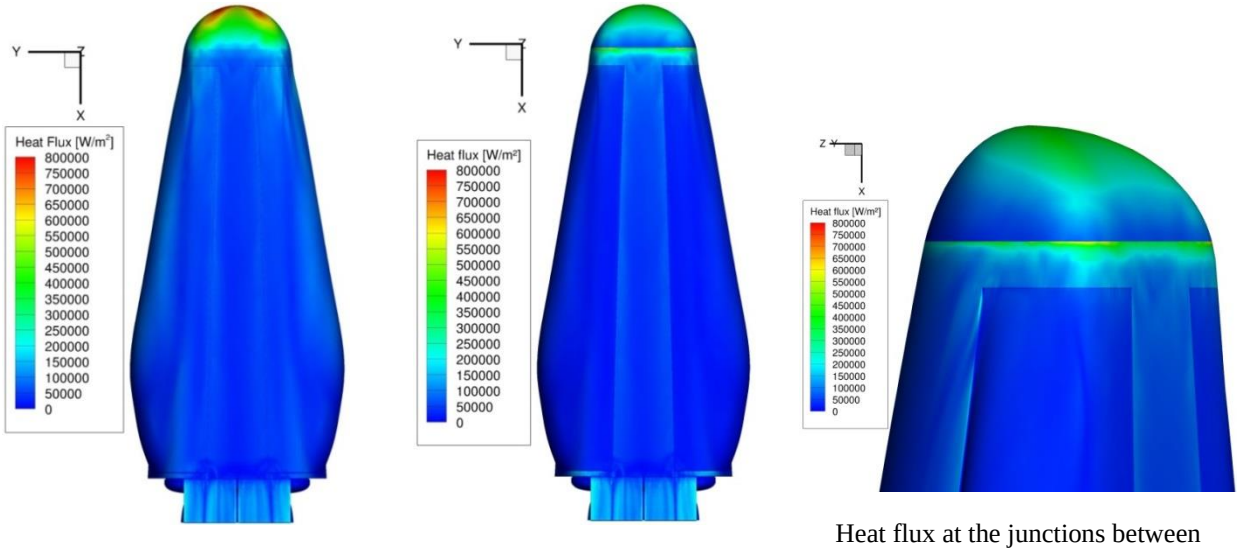

Catalytic wall Non-catalytic wall Heat flux at the junctions between catalytic/non-catalytic walls.

Figure 38: Influence of the wall catalycity on the heat flux distribution in the neighbourhood of the nose and inflatable system of the detailed geometry.

DOI: 10.13009/EUCASS2017-215

Table 1. Comparison between the stagnation point maximum heat fluxes and temperatures obtained for both catalytic and non-catalytic assumptions

	Heat flux	Temperature
Catalytic wall	808 kW/m²	2080 K
Non-catalytic wall	438 kW/m²	1762 K
Difference (%)	46%	15%

Conclusion and perspective

Regarding ATD critical issues occurring during hypersonic re-entry of the escape capsule, "high fidelity" simulations were conducted to address morphing effect of the inflated wings deployment at Mach 20 and updated heating estimate considering a flight configuration with technological effects of the vehicle at Mach 20. Moreover, during morphing phase discussion, questions raised about the potential transient effects on heating sizing policy for inflatable systems relevance. Therefore, a transient time-resolved calculation of the initial deployment of the inflatable winged devices was conducted for a limited but significant part of the deployment sequence. This simulation confirmed no transient overshoot or undershoot mechanism was observed at Mach 20 and steady-state solutions could be then applicable between initial surface and the final inflated one (as continuous sequence of growing windward surface).
Micro-aerothermodynamic simulations of a realistic vehicle including technological elements like gaps, folding cavities for rudders, stiffeners for flaps, jettisoning thrusters, etc. were performed at M = 20 involving the use of 90 Million mesh cells. These unique computations in the domain of high enthalpy flow sustained optimization investigation for the industrial design of the rescue capsule by providing updated aerodynamic and ATD predictions to partners in charge of GNC, Systems and thermal protection system (TPS).
ONERA demonstrated its ability to handle aerodynamic and aerothermodynamic issues of hypersonic flight by addressing critical process like transient morphing design or critical heating phenomena on technological elements designed for an industrial flight vehicle.

The transient calculation could be run until end of deployment (2s) to confirm CEDRE platform ability to manage larger mesh deformations. Moreover, rudders deployment would probably represent an even harder challenge due to the strong potential distortion of the mesh. More transient phenomena are probably to be expected more often in next future and investigating them would represent a breakthrough for hypersonic morphing applications. Moreover, the proper management of tremendous meshes of hundreds of millions cells, and their associated simulations, only used for classic aeronautics so far, is now required for future hypersonic planes design or RLV design due to the demand of more sophisticated databases earlier in the development phases.

Acknowledgments

The research leading to these results has received funding from the European Union's Seventh Framework Program FP7/2007-2013 under grant agreement n° ATT-2012-RTD-341531 entitled "Hypersonic Morphing for a Cabin Escape System (HYPMOCES)".

References

[1] Sippel, M., Klevanski, J., Steelant, J. 2005. Comparative Study on Options for High-Speed Intercontinental Passenger Transports: Air-Breathing vs. Rocket-Propelled. In: *56th International Astronautical Congress*.
[2] Schwanekamp, T., Bütünley, J., Sippel, M. 2012. Preliminary Multidisciplinary Design Studies on an Upgraded 100 passenger SpaceLiner Derivative. In: *18th AIAA International Space Planes and Hypersonic Systems and Technologies Conference*.
[3] Sippel, M., Bussler, L., Kopp, A., Krummen, S., Valluchi, C., Wilken, J., Prévereaud, Y., Vérant, J.-L., Laroche, E., Sourgen, F., Bonetti, D. 2017. Adanced Simulations of Reusable Hypersonic Rocket-Powered Stages. In: *21st AIAA International Space Planes and Hypersonic Systems and Technologies Conference*. AIAA 2017-2170.
[4] Laroche, E., Prévereaud, Y., Vérant, J.-L., Sourgen, F., Bonetti, D. 2015. Aerothermodynamics analysis of the SpaceLiner Cabin Escape System modified via a morphing system. In: *8th European Symposium on Aerothermodynamics for Space Vehicles*.
[5] Viladegut, A., Panerai, F., Chazot, O., Pichon, T., Bertrand, P., Verdy, C., Coddet, C. 2017. Design, integration and preliminary results of the IXV Catalysis experiment. *CEAS Space Journal*. 9:141-151.

DOI: 10.13009/EUCASS2017-215

[6] Sippel, M., Valluchi, C., Bussler, L., Kopp, A., Garbers, N., Stappert, S., Krummen, S., Wilken, J. 2017. SpaceLiner Concept as Catalyst for Advanced Hypersonic Vehicles Research. In: *7th European Conference for Aeronautics and Space Sciences*.